Applied Catalysis B: Environment and Energy 345 (2024) 123667

Contents lists available at ScienceDirect

Applied Catalysis B: Environment and Energy

journal homepage: www.elsevier.com/locate/apcatb

Surface structure regulation of sulfidated zero-valent iron by H_2O_2 for efficient pH self-regulation and proton cycle to boost heterogeneous Fenton-like reaction for pollutant control

Can Feng [a,b], Heng Zhang [a,b], Yang Liu [a,b,*], Yi Ren [c], Peng Zhou [a,b], Chuan-Shu He [a,b], Zhaokun Xiong [a,b], Weihua Liu [d], Xiaoqiang Dai [d], Bo Lai [a,b,*]

[a] State Key Laboratory of Hydraulics and Mountain River Engineering, College of Architecture and Environment, Sichuan University, Chengdu 610065, China
[b] Sino-German Centre for Water and Health Research, Sichuan University, Chengdu 610065, China
[c] State Key Laboratory of Hydraulics and Mountain River Engineering, College of Water Resource & Hydropower, Sichuan University, Chengdu 610065, China
[d] China MCC5 Group Corp., Ltd, Chengdu 610063, China

ARTICLE INFO

Keywords:
Sulfidated zero-valent iron
Proton transfer
PH self-regulation
Heterogeneous Fenton-like
Pollutant control

ABSTRACT

Sulfidated zero-valent iron (SZVI) has been widely used in controlling organic pollutants. However, the significant decrease in catalytic activity of SZVI-based Fenton-like systems under neutral and alkaline conditions remains a large problem. Herein, it was found that surface structure regulation of SZVI with H_2O_2 (HT-SZVI) greatly enhanced its reactivity and efficiently activated H_2O_2 to oxidize various organics in a wide pH range. The HT-SZVI/H_2O_2 system exhibited a pH self-regulation capability that stabilized the eventual solution pH at ~3.5 at the initial pH of 3.0–9.0. The excellent oxidation performance was primarily attributed to surface-bound $^{\bullet}OH$ produced from H_2O_2 activation by surface Fe(II) sites on HT-SZVI. Additionally, dissolved Fe(II) converted from surface Fe(II) induced proton generation to self-regulate pH. Newly formed high proton-conductive FeS and Fe_3O_4 shells accelerated the transfer of accumulated protons in solution to iron core to produce Fe(II), enabling efficient proton consumption-regeneration cycle and enhancing $^{\bullet}OH$ production.

1. Introduction

Sulfidation, with high efficiency, simple operation and low cost, is an effective strategy to improve the reactivity, utilization ratio and electron selectivity of zero-valent iron (ZVI) for removal of organics [1–7]. Furthermore, reductive sulfur species (i.e., S^{2-}, S_2^{2-} and S_n^{2-}) in sulfidated zero-valent iron (SZVI) can achieve efficient Fe(II) regeneration, leading to more efficient activation of oxidants (e.g., H_2O_2) during Fenton-like reactions [2,8]. However, the catalytic reactivity of SZVI still inevitably suffers from the limitation of pH and is unsatisfactory [9–13]. On the one hand, SZVI with poorly proton-conductive shell layers and poor dispersity cannot impel sufficient protons to transfer from solution to the iron core and produce Fe(II) under circumneutral conditions, thereby being hard to induce efficient proton cycle and Fenton-like oxidation reaction (Eqs. (1)–(3)). On the other hand, Fe(II) is susceptible to be transformed into undesirable iron oxyhydroxide (e.g., Fe_2O_3, $Fe(OH)_3$ and FeOOH) due to intrinsic instability and loses reactivity under neutral and alkaline conditions [14–16]. This is also a common problem for the Fenton and Fenton-like systems [17–22]. Accordingly, it is especially necessary to develop an efficient strategy for surmounting the pH limitation in SZVI-based Fenton-like processes.

$$Fe^0 + 2\,H^+ \rightarrow Fe(II) + H_2 \quad (1)$$

$$Fe(II) + H_2O_2 \rightarrow Fe(III) + {}^{\bullet}OH + OH^- \quad (2)$$

$$Fe(III) + 3\,H_2O \rightarrow Fe(OH)_3 + 3\,H^+ \quad (3)$$

Although it seems easy to endow the SZVI-based Fenton-like systems with high oxidizing capability by directly adjusting the harsh acidic conditions, this will greatly increase the risk of secondary pollution (e.g., iron sludge) and restrict their long-term performance and application to in situ water remediation [23–25]. Notably, ZVI sulfidation can form a conductive iron sulfide layer including FeS and FeS_2 to substitute the iron oxide passivation layer, thus efficiently enhancing the transfer

* Corresponding authors at: State Key Laboratory of Hydraulics and Mountain River Engineering, College of Architecture and Environment, Sichuan University, Chengdu 610065, China.
E-mail addresses: liuyang_scu@scu.edu.cn (Y. Liu), laibo@scu.edu.cn (B. Lai).

https://doi.org/10.1016/j.apcatb.2023.123667
Received 11 October 2023; Received in revised form 8 December 2023; Accepted 25 December 2023
Available online 27 December 2023

capability of electrons and protons to improve the catalytic reactivity of ZVI [1,9,26–28]. Moreover, the properties of conduction layer (e.g. FeS, FeS_2 and Fe_3O_4) generated by different degrees of sulfidation and oxidation also have obvious differences [28–31]. Therefore, an intelligent structure design that enhances the SZVI proton transfer may broaden the pH application range in the SZV-based Fenton-like systems. It has been reported that H_2O_2/HCl pre-corrosion of ZVI to construct a unique surface structure improved its reactivity over a wide pH range [32,33]. Undoubtedly, H_2O_2 pre-corrosion gives a window to regulate the structure properties of SZVI, thus tuning its catalytic activity and the performance of SZVI-based oxidation systems. However, the applicability by H_2O_2 pre-corrosion of SZVI to design high-activity catalysts and surmount the pH limitation has not been verified in the previous literature. Furthermore, the underlying mechanism is still poorly understood.

In particular, H_2O_2 pre-corrosion triggers structure changes of ZVI and also influence the predominant active sites (i.e., surface and dissolved Fe(II)) and their distribution in the reaction process [32,33]. Furthermore, the reduction activity of surface Fe(II) is apparently stronger than that of dissolved Fe(II) [34–36]. However, dissolved Fe(II) and its oxidative product Fe(III) can lead to noticeable variations in solution chemical properties in ZVI-based oxidation systems, especially pH [3,37–39]. It has also been reported that dissolved Fe(II) binds with iron oxides to form magnetite, which can boost the surface Fe(II) generation and electron transfer [33,38,40]. Besides, hybridized systems with Fe^0, surface Fe(II) and dissolved Fe(II) exhibited stronger reduction capability compared with non-hybrid or partial-hybrid system [32,40,41]. Hence, the functions of surface Fe(II) and dissolved Fe(II) in the SZVI-based oxidation processes remain to be systematically elucidated.

Here, a new type of high-activity SZVI (HT-SZVI) was prepared through a facile H_2O_2 treatment of mechanochemical sulfidated zero-valent iron. The general goal of this study is to construct an effective Fenton-like oxidation system with a wide pH application range and to deeply understand the reaction mechanism that H_2O_2 pre-corrosion tunes the structure characteristics and catalytic performance of SZVI. The specific goals are to: (1) analyze the effect of H_2O_2 pre-corrosion on the structure and surface properties of SZVI; (2) assess and compare the heterogeneous Fenton-like reactivity of HT-SZVI and SZVI for organic pollutants under different reaction conditions, especially initial solution pH; (3) identify the dominant reactive oxygen species (ROS) and the transformed Fe and S species to elucidate the roles of H_2O_2 pre-corrosion in heterogeneous oxidation reaction of SZVI; (4) test the durability of the HT-SZVI/H_2O_2 system in the long-term experiments and the advanced treatment performance for actual industrial wastewater.

2. Materials and methods

2.1. Chemicals and reagents

The details about the chemicals and reagents used in this study were provided in Text S1 of Supporting Information. All chemicals and reagents were used directly without further purification.

2.2. Preparation of SZVI and HT-SZVI

Sulfidated ZVI (SZVI) was synthesized by mechanically chemical ball-milling method with original microscale ZVI and sublimed sulfur powder at a molar ratio of S/Fe of 0.20 milled in a planetary ball mill at 500 rpm for 30 h. Subsequently, 2.0 g SZVI and 4.0 mL 7.5% wt·H_2O_2 solution were successively added into a 50 mL centrifuge tube. The centrifuge tube was shaken for 20 s to release the excessive pressure, after which it was sealed and stirred to completely mix with a rotator at 200 r/min for 30 min. Afterwards, the black suspension was centrifuged and washed with deionized water until the supernatant solution pH was stable and the residual H_2O_2 was negligible. Then, the solid substance was dried in a vacuum oven at 60 ℃ for 4 h and stored in an anaerobic glovebox (855 Series, Plas-Lab Inc., China). The resulting sample was denoted as HT-SZVI. Similarly, ZVI and H_2O_2 pre-corroded ZVI (HT-ZVI) were also prepared according to the aforementioned methods but without the addition of sublimed sulfur powder for comparison purpose.

2.3. Procedures of pollutant degradation

Six typical pollutants including bisphenol A (BPA), phenol (PE), naproxen (NAP), nitrobenzene (NB), norfloxacin (NOR) and sulfamethoxazole (SMX) were selected to evaluate the catalytic reactivity of the materials. Unless otherwise stated, 0.1 g/L material and 1 mM H_2O_2 were successively added into a 250 mL beaker with 150 mL 43.8 μM organic pollutants (initial solution pH 7.0) to initiate the oxidation reaction under continuous stirring (350 r/min). Samples of about 2 mL were withdrawn from the reaction solution at specific intervals, quickly filtered using a 0.22 μm PTFE syringe filter and mixed with 20 μL 0.1 M $Na_2S_2O_3$ solution for analyzing the concentration of pollutants. The used materials were recycled by a magnet, washed with deionized water and dried in a vacuum oven at 60 °C to assess the durability of materials. All treatments were performed three times. The graphs were presented with the average and error bars.

The actual industrial wastewater was collected from an industrial zone in Jiangsu province, China. The chemical properties of the wastewater were listed in Table S2. In brief, 0.5 g/L material and 5 mM H_2O_2 were successively added into a 250 mL beaker with 150 mL wastewater to trigger the reaction. The wastewater initial pH value was ~7.0 (without further adjustment). After the reaction, the samples were withdrawn and filtered through a 0.22 μm PTFE syringe filter. Then, the total organic carbon (TOC) and chemical oxygen demand (COD) were measured to evaluate the treatment performance.

2.4. Electrochemical analysis

Electrochemical analysis was performed at the Electrochemical Workstation (CHI760E, Shanghai Chenhua Instrument Co., LTD, China). Briefly, 10 mg materials (SZVI and HT-SZVI) were thoroughly mixed with 0.4 mL methanol and 30 μL nafion, followed by sonification for 20 min to disperse the material. Then, the material slurry was evenly coated on a glassy carbon electrode as the working electrode. A platinum wire electrode and an Ag/AgCl electrode were used as the auxiliary electrode and reference electrode, respectively. The electrochemical impedance spectroscopy (EIS) and Tafel curves were recorded at a scanning rate of 0.05 V/s with 0.5 M Na_2SO_4 solution as the electrolyte.

2.5. Characterization and analysis methods

Details about characterization and analysis methods were provided in Text S2-S3 of Supporting Information. The Pearson linear correlations were analyzed using SPSS software (version 19.0, SPSS Inc., Chicago, Illinois).

3. Results and discussion

3.1. Preparation and characterization of materials

The preparation procedure of H_2O_2 pre-corroded SZVI (HT-SZVI) is briefly summarized in Fig. 1a. After a facile H_2O_2 treatment and impurity removal process, a SZVI with unique structure and surface properties was successfully synthesized. As can be seen in the transmission electron microscope (TEM) images (Fig. 1b, c and S1), SZVI prepared by ball-milling presented branch-like structure with a gloomy shell and its average size was 163.59 ± 2.30 nm. The high-resolution TEM (HR-TEM) clearly showed that SZVI has lattice spacing of 0.19 nm, according with the (220) crystal facet of FeS_2 (Fig. 1d). Energy-dispersive X-ray (EDS) mapping analysis suggested that the distribution of Fe, S and O well matched with the shell structure of SZVI (Fig. 1e and S2). Different from

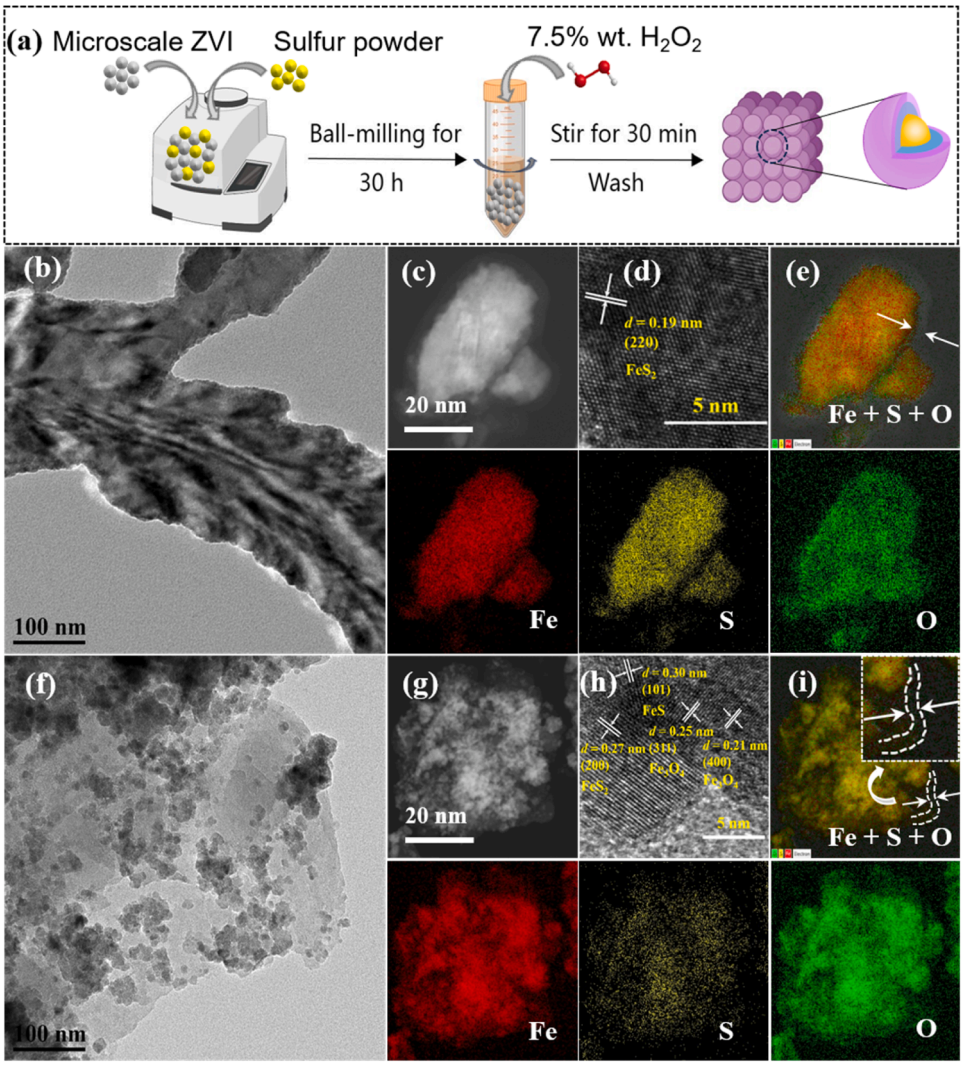

Fig. 1. (a) Schematic illustration showing the preparation of HT-SZVI. (b–c) TEM, (d) high-resolution TEM of SZVI and (e) the corresponding EDS elemental mapping of Fe, S and O as well as their overlapped images. (f–g) TEM, (h) high-resolution TEM of HT-SZVI and (i) the corresponding EDS elemental mapping of Fe, S and O as well as their overlapped images.

SZVI, HT-SZVI exhibited incompact cluster structure with a smaller particle size (21.24 ± 0.30 nm) wrapped by irregular shell (Fig. 1f, g and S1). HR-TEM further revealed that it has lattice spacing of 0.30 nm, 0.28 nm, 0.25 nm and 0.21 nm, according with the (101) facet of FeS, the (200) facet of FeS_2 as well as the (311) and (400) facets of Fe_3O_4 (Fig. 1h). The Fe + S + O overlapped elemental mapping image displayed the reservation of shell structure that composed of iron sulfides and oxides (Fig. 1i). Obviously, the H_2O_2 pre-corrosion process improved the structure of SZVI (e.g., better dispersity and smaller particle size) and regulated the surface properties of shell (e.g., roughness and conductivity).

It can be found that profited from the strong corrosion effect of H_2O_2 on SZVI, the specific surface area of HT-SZVI increased by about 25 times than SZVI (Fig. S3), which suggested more active sites exposed on the surface of HT-SZVI. Furthermore, Fe 2p X-ray photoelectron spectra (XPS) presented that Fe^0 was considerably consumed for HT-SZVI and surface Fe(II) content increased by 15.13% over SZVI (Fig. 2a and S4). Fig. S5 also showed higher content of surface Fe(II) in HT-SZVI than SZVI (close content of total Fe in them). The strong corrosion effect was further demonstrated by S 2p XPS that S^{2-} peak (161.85 eV) was newly produced after H_2O_2 pre-corrosion and the proportions of S_2^{2-} and S_n^{2-} markedly declined, whereas those of S^0, SO_3^{2-} and SO_4^{2-} increased (Fig. 2b and S4). Besides, X-ray diffraction (XRD) patterns displayed a new peak representing semiconductive Fe_3O_4 in HT-SZVI compared with the other counterpart catalysts (Fig. 2c). These characterization results confirmed the formation of FeS and Fe_3O_4. It is noteworthy that FeS and Fe_3O_4 possessed much stronger electron transfer capability than that of FeS_2 based on the band gap values (FeS_2 (0.95 eV) > Fe_3O_4 (0.1–0.3 eV) > FeS (0.1 eV)) [29,30]. Therefore, H_2O_2 pre-corrosion may improve the electron transfer capability of SZVI.

The electrochemical analysis further demonstrated that the electrons produced by Fe^0 corrosion were more prone to be transferred through the iron sulfide (i.e., FeS) and Fe_3O_4 shells of HT-SZVI in view of the much smaller semicircle diameter of HT-SZVI EIS over SZVI (Fig. 2d). This also elucidated the effectively improved proton transfer capability of HT-SZVI over SZVI because of the inverse relation between proton conductivity and electrochemical impedance [42,43]. Besides, the Tafel scanning results revealed the stronger electron transfer capability of HT-SZVI than SZVI due to the higher self-corrosion potential of HT-SZVI (–0.98 V) as against SZVI (–0.81 V) (Fig. 2e). These results agreed with the electron transfer capability (FeS_2 < Fe_3O_4 < FeS). Consequently, these critical evidences further substantiated that the shells (i.e., FeS and Fe_3O_4) with high proton conductivity and electron transfer capability were successfully formed through H_2O_2 pre-corrosion of SZVI, probably providing a high-activity reaction interface for the pollutant oxidation.

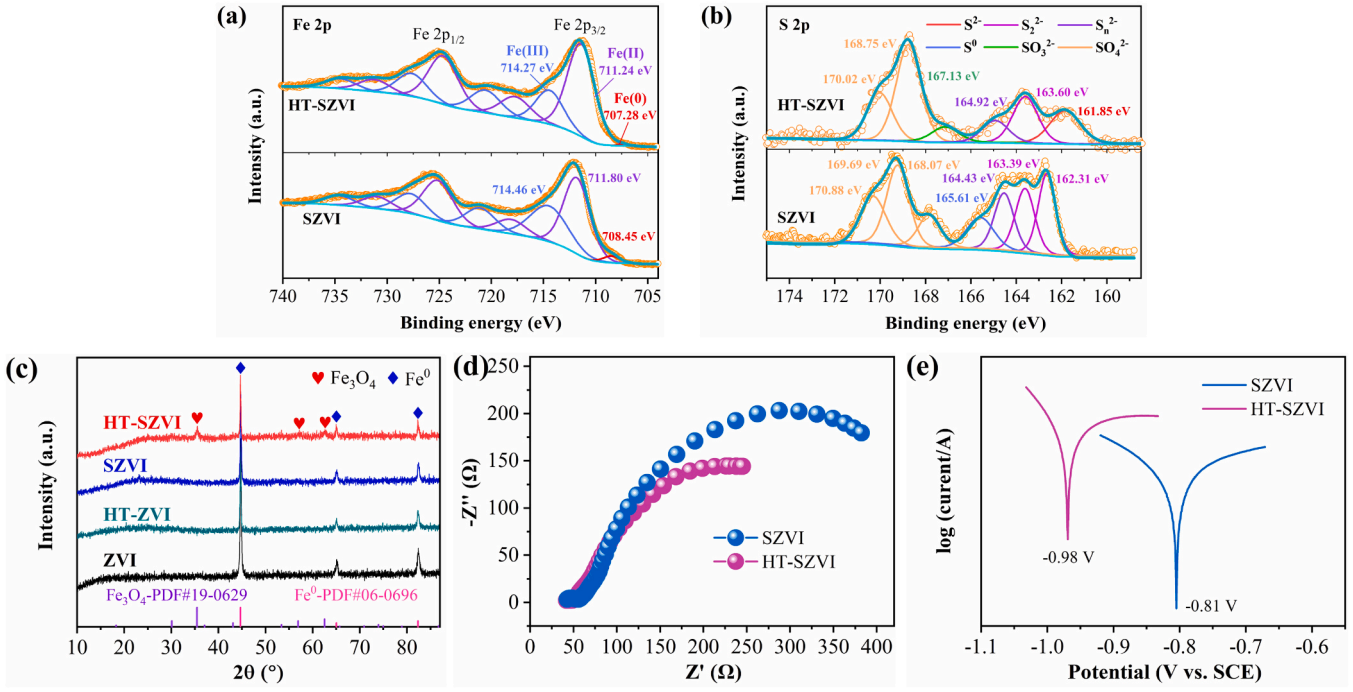

Fig. 2. (a) Fe 2p and (b) S 2p XPS spectra of SZVI before and after H_2O_2 pre-corrosion. (c) XRD patterns of ZVI and SZVI before and after H_2O_2 pre-corrosion. (d) The EIS analysis and (e) Tafel scans of SZVI and HT-SZVI.

3.2. Performance of pollutant degradation

Motivated by the above results and discussions, the performance of HT-SZVI for H_2O_2 activation to catalytic degradation of pollutants was evaluated. As presented in Fig. 3a, ZVI and SZVI before and after pre-corrosion in the absence of H_2O_2 had no oxidizing capacity for BPA. Meanwhile, ZVI, HT-ZVI and SZVI could barely activate H_2O_2 to oxidize BPA at the initial pH 7.0. However, 94% of BPA could be removed by the HT-SZVI/H_2O_2 system within 15 min (Fig. 3a). Compared with previously reported iron-based catalysts (Table S2), such as nZVI@Ti_3C_2, Cu_5/FeS_2 and nFe_2O_3/MIL-53(Cu) [44–46], HT-SZVI exhibited the higher Fenton-like reactivity to oxidize organic pollutants. In addition, the removal (50.21%) of total organic carbon (TOC) with the HT-SZVI/H_2O_2 system was 50 times higher than that (0.98%) with the SZVI/H_2O_2 system within 15 min (Fig. S6), suggesting that BPA could be effectively mineralized by the HT-SZVI/H_2O_2 system. Fig. 3b and S7 further revealed that HT-SZVI was more versatile than SZVI in efficiently oxidizing pollutants with diverse molecular structures, including phenols (PE and BPA), antibiotics (NAP, NOR and SMX) and other aromatic compounds (e.g., NB). The removal efficiencies were over 95% within

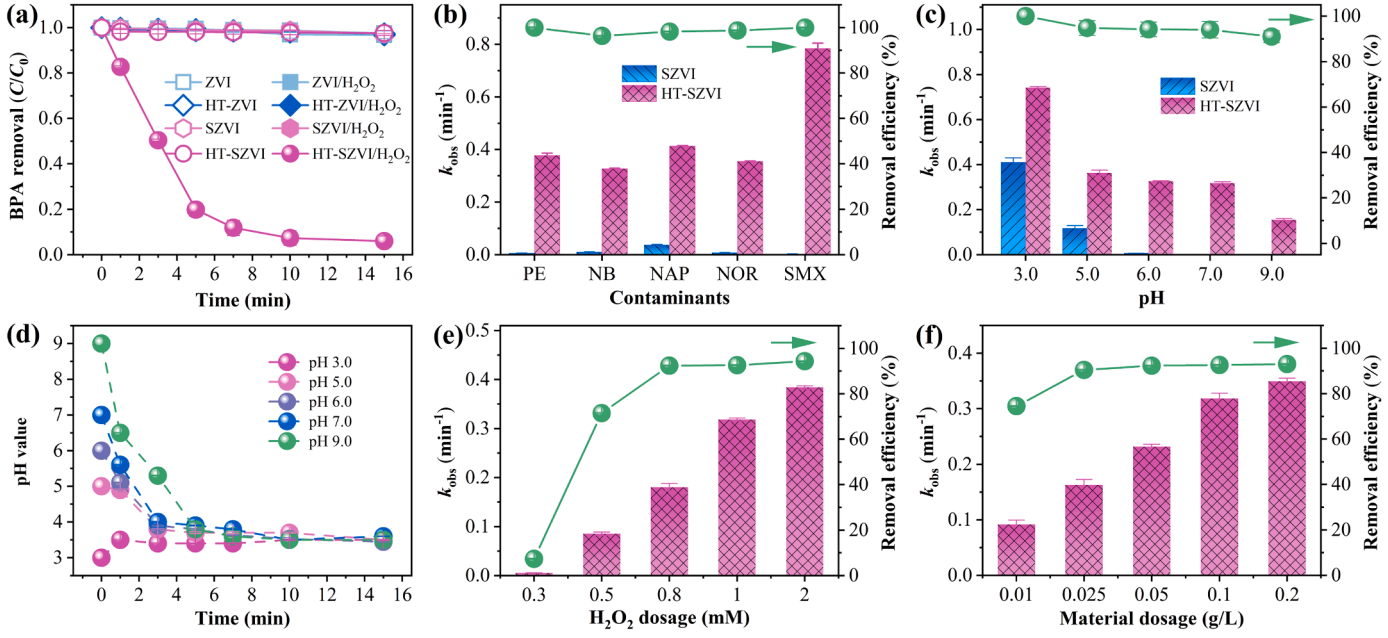

Fig. 3. (a) Removal of BPA in different activation systems. (b) Removal of different pollutants including phenol, nitrobenzene, naproxen, norfloxacin and sulfamethoxazole. (c) BPA degradation and (d) the pH evolution trends of the entire reaction process at different initial pH conditions. BPA degradation at different (e) H_2O_2 dosages and (f) material dosages. Typical conditions: $pH_0 = 7.0$, $[material]_0 = 0.1$ g/L, $[H_2O_2]_0 = 1.0$ mM, $[organic]_0 = 43.8$ μM.

15 min, displaying the universality of degradation of various organic pollutants with the HT-SZVI/H_2O_2 system.

Specially, the effects of the initial solution pH on the oxidative performance of the HT-SZVI/H_2O_2 system were evaluated. As presented in Fig. 3c and S8, the oxidizing activity of HT-SZVI/H_2O_2 system was significantly higher than SZVI/H_2O_2 system at the initial pH 3.0–9.0. Obviously, the SZVI/H_2O_2 system had a favorable BPA oxidative performance only at the initial pH of 3.0 and 5.0 (Fig. 3c and S8), which was mainly attributed to accelerated Fe^0 corrosion and Fe(II) production at a low pH. Instead, the HT-SZVI/H_2O_2 system could achieve efficient removal of BPA in the initial pH range of 3.0–9.0 and the removal efficiency reached 95–100%. Further, the pH evolution of the SZVI/H_2O_2 and HT-SZVI/H_2O_2 systems during the reaction under different initial pH conditions was monitored. Surprisingly, the solution pH values in the HT-SZVI/H_2O_2 system gradually declined over a wide initial pH range except that stepwise increased at initial pH 3.0, but eventually stabilized at about 3.5 (Fig. 3d). By contrast, the SZVI/H_2O_2 system only decreased the pH values from 9.0, 7.0, 6.0 and 5.0 to 7.1, 6.8, 5.6 and 4.9, respectively (Fig. S9). It suggested that the HT-SZVI/H_2O_2 system possessed a strong pH self-regulation capability, which enabled efficient degradation of BPA over a wide pH range. This capability possibly resulted from the pre-corrosion of SZVI by H_2O_2 to produce Fe(II) and form high proton-conductive FeS and Fe_3O_4 shells thereby boosting proton generation and transfer, which was systematically discussed in the later section. In addition, the BPA removal in the HT-SZVI/H_2O_2 system was markedly enhanced with the increase of H_2O_2 dosage (0.3–2.0 mM) and material dosage (0.01–0.20 g/L) (Fig. 3e, f and S10), chiefly related with the expedited H_2O_2 decomposition to generate more ROS. Taken together, the HT-SZVI/H_2O_2 system exhibited superior oxidative performance for organic pollutants. From the perspective of both removal performance and economy, initial pH 7.0, 0.1 g/L HT-SZVI and 1.0 mM H_2O_2 were chosen for the following experiments.

3.3. Generation and detection of ROS

To confirm the reactive oxygen species in the HT-SZVI/H_2O_2 system, quenching experiments were performed in this study. It was evident from Fig. 4a that BPA removal was almost completely inhibited by tert-butyl alcohol (TBA, for $^{\bullet}OH$) and MeOH (for $^{\bullet}OH$ and Fe^{IV}=O), but was slightly inhibited by superoxide dismutase (SOD, for $^{\bullet}O_2^-$), indicating $^{\bullet}OH$ as the dominant reactive species and the limiting role of other reactive species in the oxidation process. In fact, aqueous $^{\bullet}OH$ and surface-bound $^{\bullet}OH$ ($^{\bullet}OH_{bound}$) usually coexist during heterogeneous H_2O_2 activation process [46]. Thus, NaF was applied to identify the contribution of $^{\bullet}OH_{bound}$ to BPA degradation (Fig. 4a), since fluoride ions can desorb $^{\bullet}OH_{bound}$ through forming hydrogen bonds with HT-SZVI [47]. As presented in Fig. 4a, the BPA removal lowered from 94% to 15% after the addition of 2 mM NaF, suggesting that surface-bound $^{\bullet}OH$ played a key role in BPA degradation. Fe^{IV}=O trapping experiment and EPR measurement further affirmed the main role of $^{\bullet}OH$ due to no apparent production of $PMSO_2$ (Fig. S11) [48] and the quartet peak representing DMPO-$^{\bullet}OH$ observed in the HT-SZVI/H_2O_2 system (Fig. 4b). In addition, a much stronger DMPO-$^{\bullet}O_2^-$ signals (quartet peak with the intensity of 1:1:1:1) appeared in the HT-SZVI/H_2O_2 system than the SZVI/H_2O_2 system (Fig. 4c), indicating the production of superoxide radicals. Furthermore, the gradually enhanced HPLC peak intensity of 7-hydroxycoumarin with coumarin as the chemical probe in the HT-SZVI/H_2O_2 system suggested the production and accumulation of $^{\bullet}OH$ with the proceeding reaction (Fig. S12). Especially, the HT-SZVI/H_2O_2 system produced 11.67 μM of 7-hydroxycoumarin within 15 min, whereas only 0.24 μM of 7-hydroxycoumarin in the SZVI/H_2O_2 system was generated (Fig. 4d). The production of p-hydroxybenzoic acid (p-HBA) with benzoic acid as the chemical probe also revealed the far more generation of $^{\bullet}OH$ in the HT-SZVI/H_2O_2 system compared to the SZVI/H_2O_2 system (Fig. S13). The above critical experiments corroborated that H_2O_2 pre-corrosion of SZVI greatly improved its catalytic reactivity for H_2O_2 activation to produce $^{\bullet}OH$, especially surface-bound $^{\bullet}OH$.

3.4. Mechanism investigation

Since the distribution and content of Fe(II) species determine the

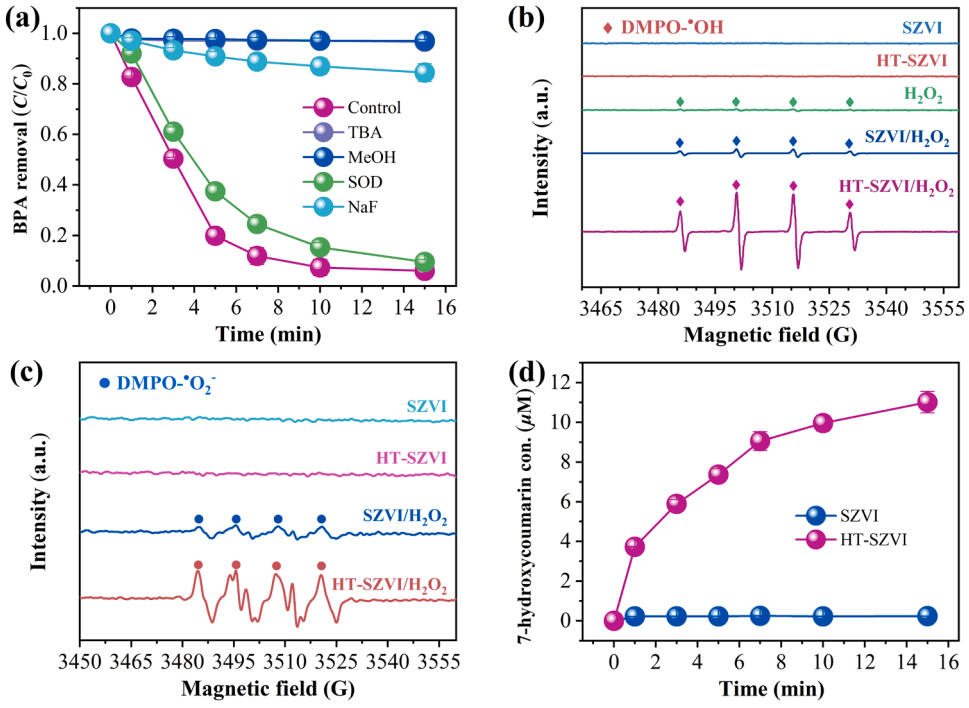

Fig. 4. (a) The quenching tests. EPR spectra of $^{\bullet}OH$ (b) and $^{\bullet}O_2^-$. (c) with DMPO addition. (d) The production of 7-hydroxycoumarin (coumarin-OH adduct). Conditions: pH_0 = 7.0, $[material]_0$ = 0.1 g/L, $[H_2O_2]_0$ = 1.0 mM. (a) $[TBA]_0$ = $[MeOH]_0$ = 10 mM, $[SOD]_0$ = 10 mg, $[NaF]_0$ = 2 mM, $[BPA]_0$ = 43.8 μM; (b) and (c) $[DMPO]_0$ = 50 mM; (d) $[coumarin]_0$ = 2 mM.

reactivity of the Fenton-like processes, the evolution of Fe(II) species was monitored. As depicted in Fig. 5a, the surface Fe(II) and dissolved Fe (II) in the HT-SZVI/H_2O_2 system both presented an obvious escalating trend as the reaction proceeded and were much higher than in the SZVI/H_2O_2 system. Meanwhile, the concentration of total Fe(III) and dissolved Fe(III) rapidly increased with the prolonged reaction duration (Fig. S14). These revealed the enhanced HT-SZVI corrosion during the oxidation process. Notably, the concentration of surface Fe(II) in the HT-SZVI/H_2O_2 system could be maintained at 0.62–0.93 mM within 1–15 min, which was always dominant in total Fe(II) (> 82%) and much more than the SZVI/H_2O_2 system (Fig. 5a). It can also be found that considerable dissolved Fe(II) (0.036–0.20 mM) produced during the first 7 min in the HT-SZVI/H_2O_2 system. By contrast, the SZVI/H_2O_2 system only produced 0.032 mM dissolved Fe(II) within 15 min. As a consequence, the H_2O_2 decomposition in the HT-SZVI/H_2O_2 system was remarkably enhanced and reached almost 100% within 15 min (Fig. 5b). In addition, Fe 2p XPS profiles of HT-SZVI also revealed that surface Fe (II) maintained a high content and increased by 4.2% after the reaction (Fig. S15). By S 2p XPS analysis, the sum percentages of S^{2-} and S_n^{2-} dropped from 23.5% to 10.1% accompanied by the increase of S_2^{2-} from 17.3% to 33.0%, implying Fe(II) regeneration probably promoted by reductive sulfide including S^{2-} and S_n^{2-} [2,49]. These evidence unraveled that H_2O_2 pre-corrosion expedited SZVI to produce surface Fe(II) and dissolved Fe(II) to catalyze H_2O_2 decomposition into $^{\bullet}OH$ throughout the oxidation process. 2,2'-bipyridine (BPY) was further added to mask the surface Fe(II) active sites in the HT-SZVI/H_2O_2 system due to its ability to complex with Fe(II) to impede electron transfer to the oxidant on the particle surface, but not to directly quench $^{\bullet}OH$ [50,51]. Impressively, BPY blocked 90% of the produced $^{\bullet}OH$ (p-HBA yield from 147 to 13 μM) and significantly inhibited the BPA degradation (removal efficiency from 94% to 37% and the rate constant from 0.319 to 0.027 min^{-1}) after the addition of 2 mM BPY (Fig. 5c and S16). This demonstrated that surface Fe(II) primarily induced the H_2O_2 activation into $^{\bullet}OH$ during the heterogeneous oxidation reaction [52], explaining why surface-bound $^{\bullet}OH$ mainly contributed to BPA degradation (Fig. 4a).

Of particular note is that the HT-SZVI/H_2O system rapidly released 0.28 mM dissolved Fe(II) before 5 min and then lowed to 0.035 mM in the absence of H_2O_2, while the SZVI/H_2O system released only 0.032 mM ferrous ions (Fig. 5d). It could be also observed to have no pH increase in HT-SZVI/H_2O system (Fig. S17). These results suggested that the initially released dissolved Fe(II) was not deriving from the Fe^0 oxidation (consumption of protons) under circumneutral conditions (Eq. (1)), but from the dissolution of surface-bound Fe(II). Because H_2O_2 pre-corrosion of SZVI facilitated part of surface Fe(II) generated during the ball-milling process more easily released into the solution to form dissolved Fe(II) [53,54]. Furthermore, the solution pH in the HT-SZVI/H_2O_2 system with and without BPA exhibited a rapid decrease to below 4.0 with time, while it had no obvious change in the HT-SZVI and SZVI systems without H_2O_2 (Fig. S17). This manifested the significant role of H_2O_2 pre-corrosion and H_2O_2 as the oxidant (Eq. (2)) in the rapid pH decrease in the HT-SZVI/H_2O_2 system. The previous studies have revealed that the presence of dissolved Fe(II) can enhance the reactivity of ZVI through two mechanisms: (i) generation of protons to reduce the solution pH via hydrolysis and the deprotonation of surface hydrous iron oxides on ZVI [3,55]; (ii) formation of magnetite by binding with iron oxides to increase the concentration of surface-bound Fe(II) and facilitate electron transfer [33,38,40]. To demonstrate this, the pH variation trends were compared with SZVI and HT-SZVI systems by mechanically mixing with Fe_3O_4 and $FeSO_4$•7 H_2O (Fig. S17). It could be noticed that the solution pH values of SZVI and Fe_3O_4 systems in the presence of $FeSO_4$•7 H_2O reduced from 7.0 to 5.8–6.1. Interestingly, the $FeSO_4$•7 H_2O/H_2O_2 and SZVI/$FeSO_4$•7 H_2O/H_2O_2 systems exhibited a sharp pH decrease, resembling the pH decrease trends in the HT-SZVI/H_2O_2 system (Fig. S17). These revealed that dissolved Fe(II) resulted in the solution pH dropping in the presence of H_2O_2 by inducing proton generation. As listed in Eqs. (2) and (3), Fe(II) activating H_2O_2 consumed protons and Fe(III) as the Fe(II) oxidation product produced substantial protons through hydrolysis, leading to a net increase of 2 moles protons per mole consumption of dissolved Fe(II). In addition, dissolved Fe(II), surface Fe(II) and magnetite in the HT-SZVI/H_2O_2 system increased after oxidation reaction (Fig. 5a and S18), indicating that H_2O_2 pre-corrosion accelerated the production of dissolved Fe(II) and subsequently the formation of magnetite. The synergistic effect of

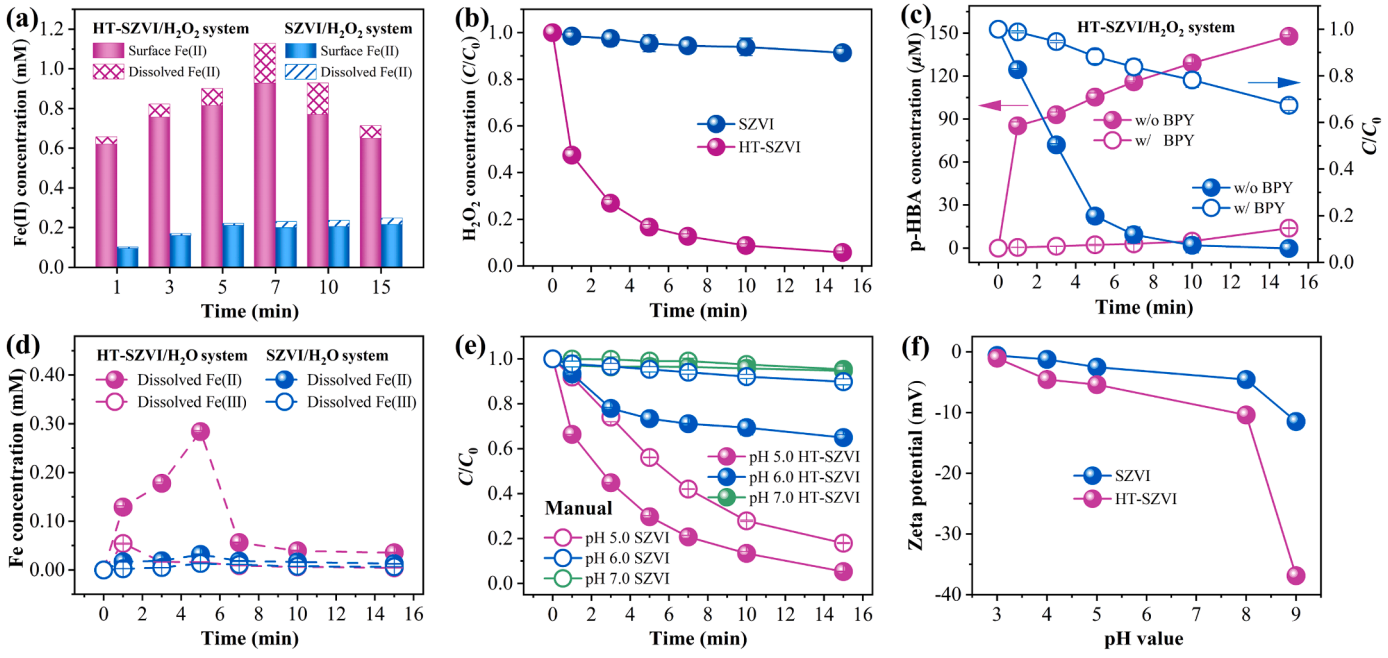

Fig. 5. (a) The concentration of Fe(II) in the SZVI/H_2O_2 and HT-SZVI/H_2O_2 systems. (b) H_2O_2 decomposition in different systems. (c) Quenching experiments for Fe (II) sites. [BPY] = 2 mM. $[BA]_0$ = 8 mM. (d) The concentration of dissolved Fe(II) and Fe(III) in the SZVI/H_2O and HT-SZVI/H_2O systems. (e) The degradation of BPA at different manually maintained pH conditions (adjusted by H_2SO_4 and NaOH). (f) Zeta potential of SZVI and HT-SZVI as a function of pH value.

dissolved Fe(II), magnetite and sulfidation could significantly enhance the SZVI reactivity [3]. Further exploring the effect of H_2O_2 on solution pH suggested that H_2O_2 only slightly decreased the pH from 7.0 to 6.3 (Fig. S19), thus ruling out the role of H_2O_2 in the noticeable reduction of the solution pH by providing protons. Consequently, dissolved Fe(II) as the key active site enabled the pH self-regulation and promoted the high reactivity of the HT-SZVI/H_2O_2 system.

To further validate the effect of the pH self-regulation, BPA degradation was performed at different manually maintained pH conditions and in buffer solutions. As expected, the SZVI/H_2O_2 and HT-SZVI/H_2O_2 systems were both hard to initiate the oxidation reaction due to the lack of protons and had a poor oxidative performance when the solution pH was manually maintained at 7.0 (Fig. 5e and S20). On the contrary, the HT-SZVI/H_2O_2 system could efficiently remove BPA in a short time at pH 5.0 and 6.0. Its oxidizing rate (k_{obs} = 0.217 and 0.050 min^{-1}) apparently outperformed the SZVI/H_2O_2 system (k_{obs} = 0.120 and 0.007 min^{-1}). The removal trends of BPA in buffer solutions were similar to those under manually maintained pH conditions (Figs. S20 and S21). As a consequence, the pH self-regulation produced a conspicuous effect on the BPA removal with the HT-SZVI/H_2O_2 system. Nevertheless, the oxidizing performance of HT-SZVI/H_2O_2 system was obviously superior to that of SZVI/H_2O_2 system under equivalent pH conditions, indicating that the enhanced BPA degradation by the HT-SZVI/H_2O_2 system could not be solely explained by the pH self-regulation.

It has been well acknowledged that protons for Fe^0 corrosion must transfer through the shells of iron sulfides and iron oxides on the surface of SZVI and HT-SZVI. Furthermore, the Fe^0 corrosion process by protons is always accompanied by the electron transfer process [39]. Thus, the proton conductivity, proton utilization and electron transfer capability of the shell can greatly affect Fe(II) production, proton cycling and radical formation. As demonstrated earlier, HT-SZVI possessed a higher proton-conductive shell and faster electron transport capacity than SZVI (Fig. 2), reflecting that it could more efficiently transfer protons to iron core and impel Fe^0 corrosion to generate Fe(II), thereby boosting proton cycling and the Fenton-like oxidation reaction. Besides, the electrons released from the proton-corroded Fe^0 process could transfer through the high proton-conductive shell to the outer ferric ions, thus achieving the efficient regeneration of surface Fe(II), which also explained why the surface Fe(II) maintained a high concentration throughout the reaction. This was similar to the mechanism of electron transfer through the crystal bulk (e.g., hematite and maghemite) proposed by previous studies [56,57]. Zeta potential further indicated that HT-SZVI carried more surface negative charge than SZVI and the isoelectric point of HT-SZVI was 2.25 (Fig. 5f). This revealed that HT-SZVI surface was electronegative across a solution pH range of 3.0–9.0, favoring proton adsorption and inward transfer to the iron core and the production of Fe (II) as well as the trapping of ferrous ions to form surface Fe(II). These evidences elucidated that the high proton-conductive shell of HT-SZVI was another important reason for boosted BPA degradation by the HT-SZVI/H_2O_2 system.

Pearson linear correlations between Fe(II) concentration and proton concentration as well as between Fe(II) concentration and BPA removal during the reaction were analyzed to further elucidate the role of surface Fe(II) and dissolved Fe(II). As evident from Fig. 6a, the surface Fe(II) concentration exhibited no significant positive correlation with proton concentration. In contrast, there was an extremely significant positive correlation between the dissolved Fe(II) and the proton concentration (Fig. 6b, $R^2 = 0.95$, $p < 0.01$). Furthermore, it could be seen that H_2O_2 decomposition showed highly significant positive correlation with surface Fe(II) concentration and no significant correlation with dissolved Fe (II) concentration (Figs. S22a and b). In addition, as expected, p-HBA production showed highly significant positive correlation with H_2O_2 decomposition and BPA removal with p-HBA production (Figs. S22c and d). As a result, the surface Fe(II) concentration had an extremely significant positive correlation with BPA removal ($R^2 = 0.95$, $p < 0.01$), whereas dissolved Fe(II) showed no significant correlation with BPA removal (Fig. 6c and d). The above evidence further revealed that dissolved Fe(II) mainly resulted in the decrease of solution pH and surface Fe(II) primarily induced H_2O_2 activation to oxidize the pollutant.

In conclusion, the mechanism of effective and rapid removal of BPA by the HT-SZVI/H_2O_2 Fenton-like system can be summarized as the following (Fig. 7): the ball-milling process of ZVI and sulfur powder could produce substantial surface-bound Fe(II) due to the formation of iron sulfide (e.g., S_2^{2-} and S_n^{2-}). The pre-corrosion of SZVI with H_2O_2

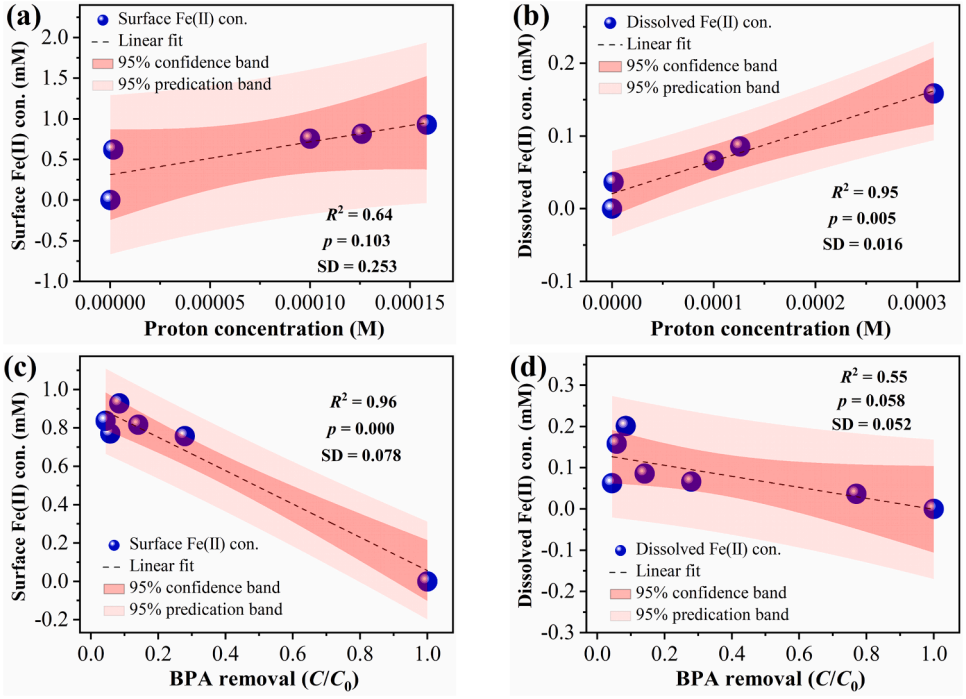

Fig. 6. The Pearson correlation analysis of Fe(II) concentration, proton concentration and BPA removal efficiency (C/C_0). p represented the significant level. SD, root mean square error, represented the deviation between the fitted value and the true value.

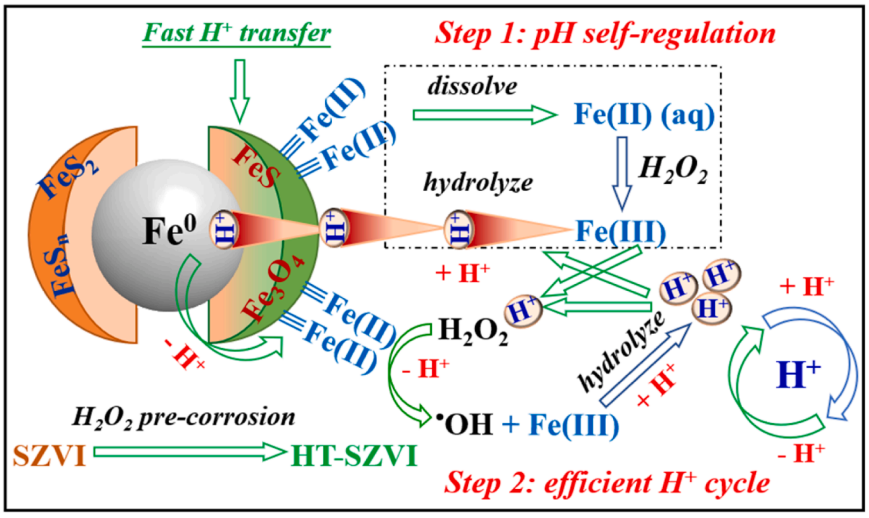

Fig. 7. Schematic diagram of the reaction mechanisms in the HT-SZVI/H_2O_2 system.

remarkably increased the concentration of surface Fe(II) and led to a looser structure and higher dispersity, thus promoting the transfer of some surface Fe(II) to solution to form dissolved Fe(II) at the initial stage of the reaction. Dissolved Fe(II) could first induce the accumulation of protons through the H_2O_2 oxidation and hydrolysis as well as deprotonation of hydrous iron oxides on the surface of HT-SZVI, resulting in the pH self-regulation of the HT-SZVI/H_2O_2 system. Meanwhile, the increase of dissolved Fe(II) accelerated the magnetite formation and surface Fe(II) production. In addition, the accumulated protons in the solution due to the pH self-regulation could easily diffuse across the high proton-conductive FeS and Fe_3O_4 shell of HT-SZVI to iron core, thus accelerating its corrosion to produce Fe(II) for H_2O_2 activation (Eqs. (1) and (2)). The released electrons could be transported through the high proton-conductive shell to the outer ferric ions and facilitated the efficient regeneration of surface Fe(II). Protons were then regenerated through hydrolysis of Fe(III) (Eq. (3)). In other words, the pH self-regulation of the HT-SZVI/H_2O_2 system maintained a low pH and the high proton-conductive shell of HT-SZVI enabled the system to achieve efficient proton cycling, while Fe^0 was continuously transformed to Fe(II) (especially surface Fe(II)) for Fenton-like oxidation of organic pollutants. The high concentration and reactivity of surface Fe(II) in HT-SZVI impelled it mainly responsible for activating H_2O_2 to produce $^{\bullet}OH$ and oxidizing pollutants. As a result, the HT-SZVI/H_2O_2 system was endowed with ultrahigh oxidation performance over a wide pH range. However, the mass and electron transfer on the SZVI were inhibited due to its intrinsic structure characteristics such as the dense structure and poor dispersity, which hindered the effective transfer of H_2O_2 or pollutants to surface Fe(II) sites and resulted in the low reactivity of SZVI at

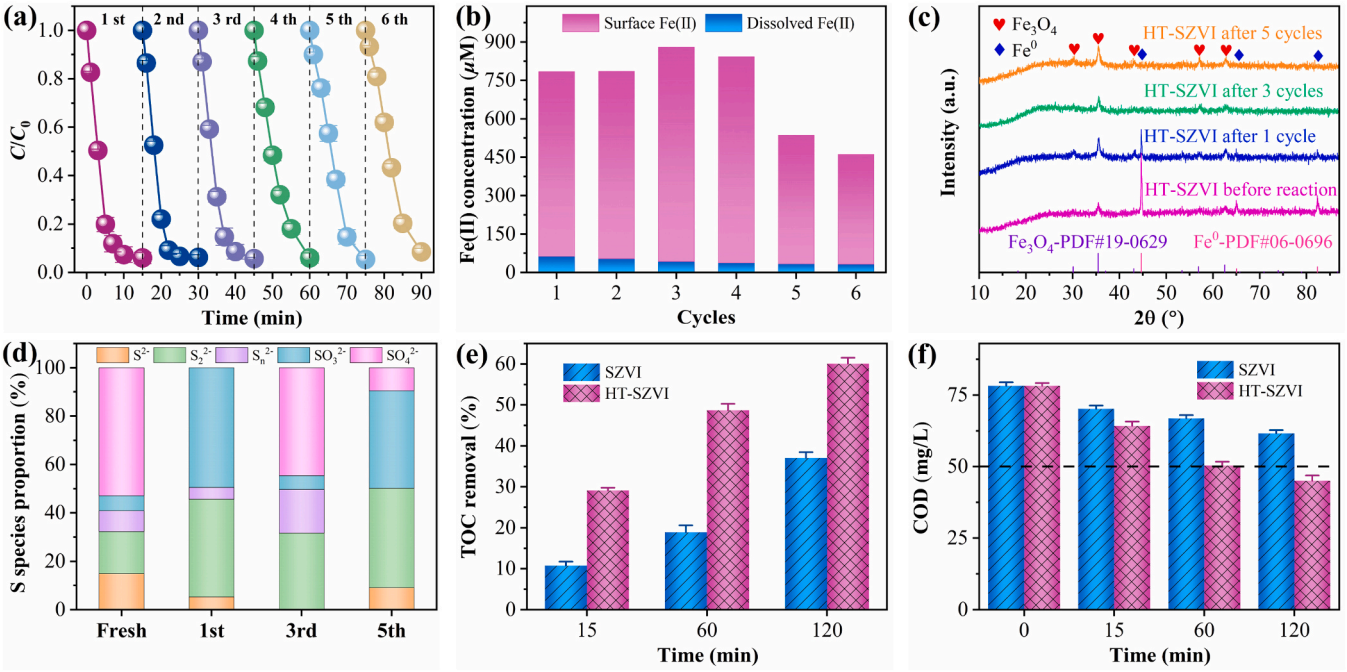

Fig. 8. (a) Cyclic degradation of BPA with HT-SZVI. (b) Fe(II) concentration after each cyclic oxidation reaction. (c) XRD pattern of HT-SZVI. (d) the proportion of S species derived from the fitting of S 2p XPS spectra after the cycle oxidation reaction. Conditions: $pH_0 = 7.0$, $[material]_0 = 0.1$ g/L, $[H_2O_2]_0 = 1.0$ mM, $[BPA]_{each\ cycle} = 43.8$ μM. (e) TOC removal and (f) COD removal for actual wastewater. The dash line marks the grade I-A level in Discharge standard of pollutants for municipal wastewater treatment plant (COD = 50 mg/L, GB18918–2002). Conditions: $pH_0 = \sim 7.0$ (without adjustment), $[material]_0 = 0.5$ g/L, $[H_2O_2]_0 = 5$ mM.

pH 7.0. Moreover, SZVI could hardly produce iron ions at the initial stage of the reaction, thereby not generating sufficient protons at pH 7.0 to cause an obvious pH decrease. Also, the poor proton conductivity of SZVI shell impeded the proton transfer from the solution to the Fe^0 core and its utilization. Thus, the SZVI/H_2O_2 system could not effectively trigger the Fenton-like oxidation reaction to remove pollutants at pH 7.0, even though a low concentration of $^{\bullet}OH$ was generated but with low activity.

3.5. Potential of practical application

Material cycling tests and actual wastewater treatment tests were conducted to confirm the practical application potential of the HT-SZVI/H_2O_2 system. It can be observed from Fig. 8a that BPA was rapidly and efficiently removed by the HT-SZVI/H_2O_2 system during the six cycles of oxidation reactions and the removal efficiencies all reached more than 92% within 15 min, indicating an excellent recyclability of HT-SZVI. Moreover, surface Fe(II) was always maintained at a high content after each oxidation reaction (Fig. 8b), which ensured sufficient active sites for H_2O_2 decomposition and $^{\bullet}OH$ production to enhance pollutant removal. According to XRD analysis, the gradually lessened Fe^0 peak and strengthened Fe_3O_4 peak of HT-SZVI samples after the cycling oxidation reaction revealed the accelerated Fe^0 corrosion to produce Fe_3O_4 for HT-SZVI (Fig. 8c). In addition, inspection of the S 2p and Fe 2p XPS profiles of HT-SZVI after successive cycles disclosed that the content of total iron sulfide (S^{2-}, S_2^{2-} and S_n^{2-}) initially increased from 40.85% to 50.54% and then remained almost unchanged (Fig. 8d), even though surface Fe(II) presented some decrease (Fig. S23). Therefore, the increase of Fe_3O_4 and iron sulfide was expected to enhance the proton conductivity of the HT-SZVI shell, thus promoting Fe^0 corrosion to produce Fe(II), continuously inducing pH self-regulation and maintaining high oxidative performance. A striking illustration of this can be seen in Fig. S24 that the solution pH values after each oxidation reaction were maintained at 3.6–3.8.

The treatment performance of actual industrial wastewater by the HT-SZVI/H_2O_2 system was further studied. Notably, the tested actual wastewater contained abundant typical anions and cations such as Cl^-, NO_3^-, SO_4^{2-}, Ca^{2+} and Mg^{2+} (Table S3). Fig. 8e showed that the TOC removal efficiency (29.7–68.6%) of the HT-SZVI/H_2O_2 system was always superior to that (10.9–37.8%) of the SZVI/H_2O_2 system within 2 h. Furthermore, the COD of wastewater decreased from 78.2 mg/L to 61.6 mg/L and 45.1 mg/L after 2 h of oxidation treatment by the SZVI/H_2O_2 and HT-SZVI/H_2O_2 systems, respectively (Fig. 8f). The level of COD by the HT-SZVI/H_2O_2 system could reach the Grade I-A of discharge standard of pollutants for municipal wastewater treatment plant (COD < 50 mg/L, GB18918–2002). These demonstrated that the HT-SZVI/H_2O_2 system was capable of effectively surmounting the interference of coexisting ions and realizing the efficient advanced treatment of actual industrial wastewater with a low concentration of COD. In summary, the long-term durability of the HT-SZVI/H_2O_2 system and its high advanced treatment performance for actual industrial wastewater highlighted the alluring potential in the practical application.

4. Conclusion

This study reported a novel SZVI catalyst with high proton-conductive shells (HT-SZVI) through a facile H_2O_2 pre-corrosion method for highly efficient degradation of organic pollutants. HT-SZVI exhibited excellent reactivity for H_2O_2 activation over a broad initial pH range of 3.0–9.0. Under these pH conditions, the strong pH self-regulation capability resulting from H_2O_2 pre-corrosion of SZVI could maintain the eventual pH of the HT-SZVI/H_2O_2 system at about 3.5. It was demonstrated that H_2O_2 pre-corrosion significantly boosted the production of surface Fe(II) sites of HT-SZVI and also enabled part of surface Fe(II) prone to form dissolved Fe(II). Dissolved Fe(II) induced the proton production to achieve the pH self-regulation, while surface Fe (II) was the dominant active site in activating H_2O_2 to produce $^{\bullet}OH$. The high proton-conductive FeS and Fe_3O_4 shells of HT-SZVI further enhanced the accumulated protons transferring to iron core and its corrosion, thus generating more Fe(II), accelerating efficient proton cycling and maintaining a low pH of the Fenton-like system. The favorable durability in the long-term experiments and efficient advanced treatment of actual industrial wastewater exhibited the great practical application potential of the novel system (HT-SZVI/H_2O_2). In conclusion, this work provided an effective strategy for surmounting pH limitation by designing high-activity SZVI to achieve effective water decontamination and deepened the understanding on the functions of surface Fe(II) and dissolved Fe(II) in Fenton-like processes.

CRediT authorship contribution statement

Lai Bo: Funding acquisition, Project administration, Resources, Writing – review & editing. **Feng Can:** Conceptualization, Formal analysis, Investigation, Methodology, Visualization, Writing – original draft. **Zhang Heng:** Funding acquisition, Methodology, Project administration, Supervision, Writing – review & editing. **Liu Yang:** Data curation, Resources, Software, Validation, Writing – review & editing. **Ren Yi:** Resources, Software, Writing – review & editing. **Zhou Peng:** Methodology, Writing – review & editing. **He Chuan-Shu:** Writing – review & editing. **Xiong Zhaokun:** Writing – review & editing. **Liu Weihua:** Resources. **Dai Xiaoqiang:** Resources.

Declaration of Competing Interest

The authors declare that they have no known competing financial interests or personal relationships that could have appeared to influence the work reported in this paper.

Data Availability

Data will be made available on request.

Acknowledgment

This work would like to appreciate the financial support from the National Natural Science Foundation of China (52070133, 52300102), the China Postdoctoral Science Foundation (2022M712233), the Natural Science Foundation of Sichuan Province (2022NSFSC1054) and the Fundamental Research Funds for the Central Universities.

Appendix A. Supporting information

Supplementary data associated with this article can be found in the online version at doi:10.1016/j.apcatb.2023.123667.

References

[1] J. Xu, A. Avellan, H. Li, X. Liu, V. Noel, Z. Lou, Y. Wang, R. Kaegi, G. Henkelman, G.V. Lowry, Sulfur loading and speciation control the hydrophobicity, electron transfer, reactivity, and selectivity of sulfidized nanoscale zerovalent iron, Adv. Mater. 32 (2020) 1906910.
[2] Y. Dai, W. Du, C. Jiang, W. Wu, Y. Dong, L. Duan, S. Sun, B. Zhang, S. Zhao, Enhanced reductive degradation of chloramphenicol by sulfidated microscale zerovalent iron: sulfur-induced mechanism, competitive kinetics, and new transformation pathway, Water Res. 233 (2023) 119743.
[3] P. Fan, Y.K. Sun, B.X. Zhou, X.H. Guan, Coupled effect of sulfidation and ferrous dosing on selenate removal by zerovalent iron under aerobic conditions, Environ. Sci. Technol. 53 (2019) 14577–14585.
[4] A.N. Garcia, Y. Zhang, S. Ghoshal, F. He, D.M. O'Carroll, Recent advances in sulfidated zerovalent iron for contaminant transformation, Environ. Sci. Technol. 55 (2021) 8464–8483.
[5] Y.Y. Zhang, P. Ozcer, S. Ghoshal, A comprehensive assessment of the degradation of C1 and C2 chlorinated hydrocarbons by sulfidated nanoscale zerovalent iron, Water Res. 201 (2021) 117328.

[6] J. Zhao, A. Su, P. Tian, X. Tang, R.N. Collins, F. He, Arsenic (III) removal by mechanochemically sulfidated microscale zero valent iron under anoxic and oxic conditions, Water Res. 198 (2021) 117132.

[7] F. Gao, H. Lyu, S. Ahmad, S. Xu, J. Tang, Enhanced reductive degradation of tetrabromobisphenol A by biochar supported sulfidated nanoscale zero-valent iron: selectivity and core reactivity, Appl. Catal. B. Environ. 324 (2023) 122246.

[8] J. Wu, J. Zhao, J. Hou, R.J. Zeng, B. Xing, Degradation of tetrabromobisphenol a by sulfidated nanoscale zerovalent iron in a dynamic two-step anoxic/oxic process, Environ. Sci. Technol. 53 (2019) 8105–8114.

[9] M.F. He, W.Q. Li, Z.H. Xie, S.R. Yang, C.S. He, Z.K. Xiong, Y. Du, Y. Liu, F. Jiang, Y. Mu, B. Lai, Peracetic acid activation by mechanochemically sulfidated zero valent iron for micropollutants degradation: enhancement mechanism and strategy for extending applicability, Water Res. 222 (2022) 118887.

[10] H. Dong, B. Wang, L. Li, Y. Wang, Q. Ning, R. Tian, R. Li, J. Chen, Q. Xie, Activation of persulfate and hydrogen peroxide by using sulfide-modified nanoscale zero-valent iron for oxidative degradation of sulfamethazine: a comparative study, Sep. Purif. Technol. 218 (2019) 113–119.

[11] J. Chen, G. Zhou, R. Ding, Q. Li, H. Zhao, Y. Mu, Ferrous ion enhanced Fenton-like degradation of emerging contaminants by sulfidated nanosized zero-valent iron with pH insensitivity, J. Hazard. Mater. 459 (2023) 132229.

[12] G. Zhou, J. Chen, C. He, R. Ding, Y. Mu, Nano-sized zero-valent iron coupled with sulfidation and ferrous implantation enhances the reduction–oxidation removal of iodinated contrast medium, ACS EST Water 1 (2021) 2128–2138.

[13] D. Li, Y. Zhong, H. Wang, W. Huang, P. Peng, Remarkable promotion in particle dispersion and electron transfer capacity of sulfidated nano zerovalent iron by coating alginate polymer, Sci. Total Environ. 759 (2021) 143481.

[14] Y. Feng, C. Liao, L. Kong, D. Wu, Y. Liu, P.H. Lee, K. Shih, Facile synthesis of highly reactive and stable Fe-doped g-C_3N_4 composites for peroxymonosulfate activation: a novel nonradical oxidation process, J. Hazard. Mater. 354 (2018) 63–71.

[15] H. Li, C. Shan, B. Pan, Development of Fe-doped g-C_3N_4/graphite mediated peroxymonosulfate activation for degradation of aromatic pollutants via nonradical pathway, Sci. Total Environ. 675 (2019) 62–72.

[16] S. Zou, Q. Chen, Y. Liu, Y. Pan, G. Yao, Z. Pan, B. Lai, The capacity and mechanisms of various oxidants on regulating the redox function of ZVI, Chin. Chem. Lett. 32 (2021) 2066–2072.

[17] H. Yin, J. Li, H. Yan, H. Cai, Y. Wan, G. Yao, Y. Guo, B. Lai, Activation of peroxymonosulfate by $CuCo_2O_4$ nano-particles towards long-lasting removal of atrazine, Water Reuse 11 (2021) 542–559.

[18] H. Li, C. Shan, B. Pan, Fe(III)-doped g-C_3N_4 mediated peroxymonosulfate activation for selective degradation of phenolic compounds via high-valent iron-oxo species, Environ. Sci. Technol. 52 (2018) 2197–2205.

[19] J.J. Pignatello, E. Oliveros, A. Mackay, Advanced oxidation processes for organic contaminant destruction based on the Fenton reaction and related chemistry, Crit. Rev. Environ. Sci. Technol. 36 (2006) 1–84.

[20] S. Yu, Z. Xie, X. Yu Wu, Y. Zheng, Y. Shi, Z. Xiong, P. Zhou, Y. Liu, C. He, Z. Pan, K. Wang, B. Lai, Review of advanced oxidation processes for treating hospital sewage to achieve decontamination and disinfection, Chin. Chem. Lett. 35 (2024) 108714.

[21] P. Zhou, W. Ren, G. Nie, X. Li, X. Duan, Y. Zhang, S. Wang, Fast and long-lasting iron(III) reduction by boron toward green and accelerated Fenton chemistry, Angew. Chem. Int. Ed. 59 (2020) 16517–16526.

[22] Y. Zhou, G. Zhang, J. Zou, Photoelectrocatalytic generation of miscellaneous oxygen-based radicals towards cooperative degradation of multiple organic pollutants in water, Water Reuse 11 (2021) 531–541.

[23] C.J. Lin, S. Lo, Effects of iron surface pretreatment on sorption and reduction kinetics of trichloroethylene in a closed batch system, Water Res 39 (2005) 1037–1046.

[24] X. Guan, Y. Sun, H. Qin, J. Li, I. Lo, D. He, H. Dong, The limitations of applying zero-valent iron technology in contaminants sequestration and the corresponding countermeasures: The development in zero-valent iron technology in the last two decades (1994–2014), Water Res 75 (2015) 224–248.

[25] J. Zhao, Q. Wu, Y. Tang, J. Zhou, H. Guo, Tannery wastewater treatment: conventional and promising processes, an updated 20-year review, J. Leather Sci. Eng 4 (2022) 1–22.

[26] J. Xu, A. Avellan, H. Li, E.A. Clark, G. Henkelman, R. Kaegi, G.V. Lowry, Iron and sulfur precursors affect crystalline structure, speciation, and reactivity of sulfidized nanoscale zerovalent iron, Environ. Sci. Technol. 54 (2020) 13294–13303.

[27] A. Nunez Garcia, H.K. Boparai, A.I.A. Chowdhury, C.V. de Boer, C.M.D. Kocur, E. Passeport, B. Sherwood Lollar, L.M. Austrins, J. Herrera, D.M.O. Carroll, Sulfidated nano zerovalent iron (S-nZVI) for in situ treatment of chlorinated solvents: a field study, Water Res. 174 (2020) 115594.

[28] F. Gao, M. Zhang, X. Yang, S. Ahmad, J. Tang, Post-sulfidation of biochar supported nanoscale zero-valent iron with different sulfur precursors: reactivity and selectivity on tetrabromobisphenol A reduction, Chem. Eng. J. 461 (2023) 141953.

[29] Y. Xu, M.A.A. Schoonen, The absolute energy positions of conduction and valence bands of selected semiconducting minerals, Am. Miner. 85 (2000) 543–556.

[30] X. Li, J. Peng, R. Liu, J. Liu, T. Feng, A. Qyyum, C. Gao, M. Xue, J. Zhang, Fe_3O_4 nanoparticle-enabled mode-locking in an erbium-doped fiber laser, Front. Optoelectron. 13 (2020) 149–155.

[31] Y. Mo, J. Xu, L. Zhu, Molecular structure and sulfur content affect reductive dechlorination of chlorinated ethenes by sulfidized nanoscale zerovalent iron, Environ. Sci. Technol. 56 (2022) 5808–5819.

[32] Z. Yang, C. Shan, Y. Mei, Z. Jiang, X. Guan, B. Pan, Improving reductive performance of zero valent iron by H_2O_2/HCl pretreatment: a case study on nitrate reduction, Chem. Eng. J. 334 (2018) 2255–2263.

[33] C. Shan, J.J. Chen, Z. Yang, H.C. Jia, X.H. Guan, W.M. Zhang, B.C. Pan, Enhanced removal of Se(VI) from water via pre-corrosion of zero-valent iron using H_2O_2/HCl: effect of solution chemistry and mechanism investigation, Water Res. 133 (2018) 173–181.

[34] J.Z. Huang, A. Jones, T.D. Waite, Y.L. Chen, X. Huang, K.M. Rosso, A. Kappler, M. Mansor, P.G. Tratnyek, H. Zhang, Fe(II) redox chemistry in the environment, Chem. Rev. 121 (2021) 8161–8233.

[35] K. Pecher, S.B. Haderlein, R.P. Schwarzenbach, Reduction of polyhalogenated methanes by surface-bound Fe(II) in aqueous suspensions of iron oxides, Environ. Sci. Technol. 36 (2002) 1734–1741.

[36] C.A. Gorski, R. Edwards, M. Sander, T.B. Hofstetter, S.M. Stewart, Thermodynamic characterization of iron oxide–aqueous Fe^{2+} redox couples, Environ. Sci. Technol. 50 (2016) 8538–8547.

[37] L. Lin, X. Hu, J. Liang, Z. Huang, G. Yu, Y. Chong, Adsorption of tylosin in wastewater by iron-rich farmland soil and the effect of iron reduction and common cations, Water Reuse 11 (2021) 248–256.

[38] H. Qin, J. Li, H. Yang, B. Pan, W. Zhang, X. Guan, Coupled effect of ferrous ion and oxygen on the electron selectivity of zerovalent iron for selenate sequestration, Environ. Sci. Technol. 51 (2017) 5090–5097.

[39] X. Zhang, H.W. Sun, Y.B. Shi, C. Ling, M. Li, C. Liang, F. Jia, X. Liu, L. Zhang, Z. Ai, Oxalated zero valent iron enables highly efficient heterogeneous Fenton reaction by self-adapting pH and accelerating proton cycle, Water Res 235 (2023) 119828.

[40] C. Tang, Y. Huang, Z. Zhang, J. Chen, H. Zeng, Y.H. Huang, Rapid removal of selenate in a zero-valent iron/Fe_3O_4/Fe^{2+} synergetic system, Appl. Catal. B. Environ. 184 (2016) 320–327.

[41] C. Shan, J. Chen, Z. Yang, H. Jia, X. Guan, W. Zhang, B. Pan, Enhanced removal of Se(VI) from water via pre-corrosion of zero-valent iron using H_2O_2/HCl: effect of solution chemistry and mechanism investigation, Water Res. 133 (2018) 173–181.

[42] S. Bureekaew, S. Horike, M. Higuchi, M. Mizuno, T. Kawamura, D. Tanaka, N. Yanai, S. Kitagawa, One-dimensional imidazole aggregate in aluminium porous coordination polymers with high proton conductivity, Mater. Sustain. Energ. 8 (2010) 232–237.

[43] Y. Hu, G. Zhan, X. Peng, X. Liu, Z. Ai, F. Jia, S. Cao, F. Quan, W. Shen, L. Zhang, Enhanced Cr(VI) removal of zero-valent iron with high proton conductive $FeC_2O_4{\cdot}2H_2O$ shell, Chem. Eng. J. 389 (2020) 124414.

[44] Y. Ren, M. Shi, W. Zhang, D.D. Dionysiou, J. Lu, C. Shan, Y. Zhang, L. Lv, B. Pan, Enhancing the Fenton-like catalytic activity of nFe_2O_3 by MIL-53(Cu) support: a mechanistic investigation, Environ. Sci. Technol. 54 (2020) 5258–5267.

[45] C. Ling, X. Liu, H. Li, X. Wang, H. Gu, K. Wei, M. Li, Y. Shi, H. Ben, G. Zhan, C. Liang, W. Shen, Y. Li, J. Zhao, L. Zhang, Atomic-layered Cu_5 nanoclusters on FeS_2 with dual catalytic sites for efficient and selective H_2O_2 activation, Angew. Chem. Int. Ed. 61 (2022) e202200670.

[46] Y.Y. Ma, X.F. Lv, D.B. Xiong, X.S. Zhao, Z.H. Zhang, Catalytic degradation of ranitidine using novel magnetic Ti_3C_2-based MXene nanosheets modified with nanoscale zero-valent iron particles, Appl. Catal. B. Environ 284 (2021) 119720.

[47] Y. Xu, K. Lv, Z. Xiong, W. Leng, W. Du, D. Liu, X. Xue, Rate enhancement and rate inhibition of phenol degradation over irradiated anatase and rutile TiO_2 on the addition of NaF: new insight into the mechanism, J. Phys. Chem. C. 111 (2007) 19024–19032.

[48] Z. Wang, W. Qiu, S. Pang, Y. Gao, Y. Zhou, Y. Cao, J. Jiang, Relative contribution of ferryl ion species (Fe(IV)) and sulfate radical formed in nanoscale zero valent iron activated peroxydisulfate and peroxymonosulfate processes, Water Res 172 (2020) 115504.

[49] C. Feng, H. Zhang, Y. Ren, M. Luo, S. Yu, Z. Xiong, Y. Liu, P. Zhou, B. Lai, Enhancing zerovalent iron-based Fenton-like chemistry by copper sulfide: Insight into the active sites for sustainable Fe(II) supply, J. Hazard. Mater. 452 (2023) 131355.

[50] W. Liu, Z. Ai, M. Cao, L. Zhang, Ferrous ions promoted aerobic simazine degradation with Fe@Fe_2O_3 core–shell nanowires, Appl. Catal. B. Environ. 150-151 (2014) 1–11.

[51] G. Fang, D.D. Dionysiou, S.R. Al-Abed, D. Zhou, Superoxide radical driving the activation of persulfate by magnetite nanoparticles: Implications for the degradation of PCBs, Appl. Catal. B. Environ. 129 (2013) 325–332.

[52] X. Guo, Z. Yang, H. Dong, X. Guan, Q. Ren, X. Lv, X. Jin, Simple combination of oxidants with zero-valent-iron (ZVI) achieved very rapid and highly efficient removal of heavy metals from water, Water Res. 88 (2016) 671–680.

[53] Z. Zhao, S. Peng, C. Ma, C. Yu, D. Wu, Redox behavior of secondary solid iron species and the corresponding effects on hydroxyl radical generation during the pyrite oxidation process, Environ. Sci. Technol. 56 (2022) 12635–12644.

[54] Y. Zhang, Z. Duan, Y. Jin, H. Han, C. Xu, Chemical bond bridging across two domains: Generation of Fe(II) and in situ formation of FeS_x on zerovalent iron, Environ. Sci. Technol. 57 (2023) 11336–11344.

[55] T. Liu, X. Li, T.D. Waite, Depassivation of aged Fe^0 by divalent cations: correlation between contaminant degradation and surface complexation constants, Environ. Sci. Technol. 48 (2014) 14564–14571.

[56] J.E. Katz, X. Zhang, K. Attenkofer, K.W. Chapman, C. Frandsen, P. Zarzycki, K. M. Rosso, R.W. Falcone, G.A. Waychunas, B. Gilbert, Electron small polarons and their mobility in iron (oxyhydr)oxide nanoparticles, Science 337 (2012) 1200–1203.

[57] S.V. Yanina, K.M. Rosso, Linked reactivity at mineral-water interfaces through bulk crystal conduction, Science 320 (2008) 218–222.